Modeling the ENSO impact of orbitally induced mean state climate changes

O. R. Salau,[1] B. Schneider,[1] W. Park,[2] V. Khon,[1] and M. Latif[2]

Received 11 November 2011; revised 10 April 2012; accepted 12 April 2012; published 30 May 2012.

[1] The sensitivity of the El Niño–Southern Oscillation (ENSO) phenomenon to changes in the tropical Pacific mean climate is investigated with a coupled atmosphere-ocean-sea ice general circulation model (AOGCM), the Kiel Climate Model (KCM). Different mean climate states are generated by changing the orbital forcing that causes a redistribution of solar energy, which was a major driver of both the Holocene and the Eemian climates. We find that the ENSO amplitude is positively correlated with both the Equatorial Pacific sea surface temperature (SST) and the equatorial zonal SST contrast. The latter is controlled by the upwelling-induced damping of the SST changes in the Eastern Equatorial Pacific (EEP), and by the vertical ocean dynamical heating and zonal heat transport convergence in the Western Equatorial Pacific. The ENSO amplitude also correlates positively with the seasonal SST amplitude in the EEP and negatively with the strength of the easterly Trades over the Equatorial Pacific. However, the ENSO period is rather stable and stays within 3–4 years. Enhanced ENSO amplitude is simulated during the late-Holocene, in agreement with paleoproxy records. The tight positive correlation (r = 0.89) between the ENSO strength and the Western Pacific Warm Pool (WPWP) SST suggests that the latter may provide an indirect measure of the ENSO amplitude from proxy data that cannot explicitly resolve interannual variability.

Citation: Salau, O. R., B. Schneider, W. Park, V. Khon, and M. Latif (2012), Modeling the ENSO impact of orbitally induced mean state climate changes, *J. Geophys. Res.*, *117*, C05043, doi:10.1029/2011JC007742.

1. Introduction

[2] The El Niño–Southern Oscillation (ENSO) is a natural interannual climate fluctuation originating in the tropical Pacific Ocean, which affects climate worldwide through atmospheric teleconnections [*Philander*, 1990; *McPhaden et al.*, 1998]. ENSO is associated with anomalous regional wind, precipitation and temperature patterns [*Ropelewski and Halpert*, 1996] that change upper ocean stratification and vertical motion, and thus nutrient conditions [*Stenseth et al.*, 2002]. The phenomenon influences not only climate and biosphere, but also the economies of several countries through impacts on agriculture and fisheries, thereby affecting human societies in many different ways [*McPhaden et al.*, 2006; *Chavez et al.*, 1999]. Hence, reliable projections of ENSO characteristics under different future greenhouse gas emission scenarios are highly desirable. State-of-the-art coupled atmosphere-ocean general circulation models (AOGCMs) are becoming better at reproducing observed patterns of interannual climate variability, including ENSO, for which the driving physical mechanisms are increasingly well understood [*Guilyardi et al.*, 2009]. However, future projections of both ENSO amplitude and frequency for the 21st century are also highly uncertain [*Collins et al.*, 2010; *Guilyardi*, 2006].

[3] Important insights into the mechanisms underlying internal climate variability and externally driven climate change may be obtained from reconstructions of past climate conditions. In particular, past warm climates may serve as analogues for future warming in response to enhanced greenhouse gas concentrations. For example, several reconstructions for the Holocene climate (last 10 kyr BP) agree that ENSO amplitude was weaker during the early to mid-Holocene compared to the present climate. Evidence comes from layers of inorganic debris deposits in lake sediments from Ecuador, which indicates a switch toward more frequent strong El Niños around 7 kyr BP [*Rodbell et al.*, 1999]. In the Indo-Pacific Warm Pool (IPWP), $\delta^{18}O$ and Sr/Ca data from corals, recording salinity (precipitation) and temperature variations, respectively, have shown increasing ENSO strength toward the end of the Holocene [*Tudhope et al.*, 2001]. The data revealed a considerably higher variability at modern times compared to the last glacial and interglacial periods (~20 and 130 kyr BP) [*Tudhope et al.*, 2001; *Moy et al.*, 2002; *Gagan et al.*, 2004]. Similarly, pollen records from northern Australia show a period of less variable conditions around 4 kyr BP, indicative of weaker ENSO variability, followed by a switch back to a drier

[1]Institute of Geosciences, University of Kiel, Kiel, Germany.
[2]GEOMAR, Helmholtz Centre for Ocean Research Kiel, Kiel, Germany.

Corresponding author: O. R. Salau, Institute of Geosciences, University of Kiel, Ludewig-Meyn-Str. 10, Kiel D-24118, Germany. (os@gpi.uni-kiel.de)

Copyright 2012 by the American Geophysical Union.
0148-0227/12/2011JC007742

(El Niño-like) state thereafter [*Shulmeister and Lees*, 1995]. Models simulating the climate of the Holocene also support the tendency of damped ENSO-related variability during the mid-Holocene [*Clement et al.*, 2000; *Liu et al.*, 2000; *Otto-Bliesner et al.*, 2003; *Brown et al.*, 2006]. The damping is mostly explained by the effect of a precession-induced strong enhancement of the Asian Monsoon [*Zheng et al.*, 2008; *Kutzbach and Liu*, 1997].

[4] In general, the Eemian (~130 to 116 kyr BP) experienced a warmer climate than today [*Jansen et al.*, 2007] probably with significantly reduced Northern Hemisphere ice volume [*Stirling et al.*, 1998; *Otto-Bliesner et al.*, 2006]. Both periods (Holocene, Eemian) are within the well-dated 150 kyr BP interval over which a meaningful test of the orbital theory could be made with a good accuracy in the geological chronology [*Hays et al.*, 1976]. Comparable orbital configurations and tropical warming trends of both periods [*Leduc et al.*, 2010] make them suitable examples to test the effect of orbitally induced changes in the mean state of the tropical Pacific on ENSO.

[5] ENSO is a complex internal climate fluctuation that is usually explained by either a naturally sustained oscillation or by a damped mode forced by atmospheric noise [*Neelin et al.*, 1998; *Wang and Picaut*, 2004; *Fedorov and Philander*, 2000; *McWilliams and Gent*, 1978; *Lau*, 1985; *Kleeman and Moore*, 1997; *Penland and Sardeshmukh*, 1995; *Eckert and Latif*, 1997; *Kessler*, 2002; *Moore and Kleeman*, 1999; *Thompson and Battisti*, 2001; *Dijkstra and Burgers*, 2002; *Larkin and Harrison*, 2002; *Zavala-Garay et al.*, 2003; *Blanke et al.*, 1997]. Some robust relationships between ENSO and the mean tropical Pacific climate state were derived from the current generation of climate models [*Guilyardi*, 2006], which are supported by 1000 years of tree ring data from the North American continent [*Li et al.*, 2011]. For example, ENSO strength in the models has been shown to be an inverse function of the mean trade wind strength in the Central Equatorial Pacific as well as of the relative strength of the seasonal cycle in the Eastern Equatorial Pacific (EEP). Changes of the mean state also affect the feedback loops such that in a warm climate, for instance, SST sensitivity is amplified due to an increased sharpness of the thermocline. However, various competing processes act at the same time so that it is difficult to anticipate the net effect of future expected warming [*Philip and van Oldenborgh*, 2006]. Nevertheless, the results from climate model simulations are important to understand the effect of mean state changes on ENSO and ocean-atmosphere feedbacks in the Tropics. Paleoproxies often do not permit the reconstruction of seasonal to interannual variability, which is mainly due to a lack of sufficient temporal resolution and/or proxy sensitivity [*Intergovernmental Panel on Climate Change*, 2007; *Leduc et al.*, 2010]. Therefore, forming a robust link between ENSO and the mean state could allow proxy records with coarse time resolution to provide a strong constraint on reconstructions of ENSO during past climates.

[6] To investigate the relationship between ENSO and the mean climate state in the tropical Pacific across different warm climate intervals, we use in the present study a state-of-the-art AOGCM that is forced by changes in the orbital parameters (eccentricity, obliquity, precession) as occurred during the Holocene and the Eemian. Section 2 describes the model and the configuration of the simulations. The model performance and sensitivity to external forcing, as well as the mechanisms that control the changes in ENSO variability are described in section 3. A discussion of the most important results and the major conclusions are presented in sections 4 and 5, respectively.

2. Model and Experiments

[7] We use a fully coupled atmosphere-ocean-sea ice general circulation, the Kiel Climate Model (KCM) [*Park et al.*, 2009]. The atmospheric component is ECHAM5, the Hamburg (Max Planck Institute for Meteorology) atmospheric general circulation model version 5 [*Roeckner et al.*, 2003], with a T31 resolution (3.75° × 3.75°) horizontally and 19 vertical levels. The ocean model is OPA9 [*Madec*, 2008] which is run here on a 2° Mercator mesh with enhanced meridional resolution of 0.5° in the equatorial region and 31 vertical levels that are unevenly spaced with a grid distance ranging from 10 m in the upper 100 m to 500 m below. The sea-ice model LIM2 [*Fichefet and Morales Maqueda*, 1997] is coupled to OPA9 and runs on the ocean grid.

[8] The ocean and atmosphere models are coupled via the coupler OASIS3 [*Valcke*, 2006]. The coupled model does not use flux correction, and it has previously been shown to realistically reproduce the present-day climate and global ocean circulation [*Park and Latif*, 2008; *Park et al.*, 2009]. In particular, the annual mean state, semi-annual and annual cycle, together with the interannual variability are simulated well in the tropical Pacific. Also, the KCM simulates the characteristics of the internal climate variability such as the Pacific Decadal Variability and Atlantic Multidecadal Variability comparable to the observations in terms of spatial and temporal structure [*Park and Latif*, 2010]. The response of the KCM to periodic multidecadal and centennial solar forcing is examined by *Park and Latif* [2012]. More details including the KCM's performance of the modern mean state and variability, and the model's response to enhanced CO_2 can be found in *Park et al.* [2009].

[9] In the present study, six quasi-steady state (time-slice) experiments are performed with prescribed orbital configurations for the parameters eccentricity, obliquity and precession, representing distinct time periods during two warm climates, the Holocene (9.5 kyr BP, 6 kyr BP, preindustrial) and the Eemian (126 kyr BP, 122 kyr BP, 115 kyr BP) (Figure 1 and Table 1) [see also *Braconnot et al.*, 2008; *Schneider et al.*, 2010; *Khon et al.*, 2010]. Both warm periods underwent similar transient changes of the orbital parameters. For example, obliquity decreased over time while the precessional index increased during both epochs. Overall, eccentricity was about two times higher during the Eemian compared to the Holocene; it slightly increased during the Eemian, whereas it decreased during the Holocene (Table 1). Precessionally pair-wise similar experiments are performed for the respective early, middle and late phases of both periods (Figure 1). Although the global annual mean insolation remained virtually constant for all time periods, the resulting seasonal and latitudinal insolation changes during the Eemian were about twice as large as during the Holocene.

[10] The simulations follow the standard protocol of the Paleo-Modeling Intercomparison Project (PMIP) [*Joussaume and Taylor*, 1995; *Braconnot et al.*, 2008], where the orbital parameters were computed according to *Berger* [1978]. During the Holocene, factors other than orbital forcing are

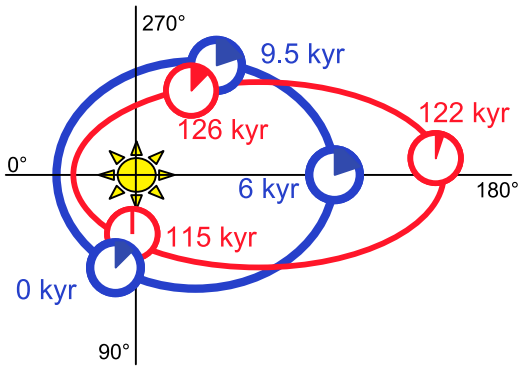

Figure 1. Sketch illustrating the solar constellations of the different time periods used in the present study (adapted from *Braconnot et al.* [2008]). Shown is the location of the vernal equinox on the Earth's orbit around the Sun (first day of the spring; March 20 in the Northern Hemisphere). Blue and red orbits represent the Holocene and Eemian epochs, respectively. The wedges roughly sketch relative changes in obliquity.

assumed to be of minor importance. However, the neglect of changes in sea level and ice sheet extent is probably oversimplified for the Eemian [*Otto-Bliesner et al.*, 2006], while the role of dynamic vegetation during the mid-Holocene is still under debate [*Ganopolski et al.*, 1998; *Zeng and Neelin*, 2000]. Consequently, this study is rather a sensitivity study, testing the response of a climate model to changes in the orbital configurations including sea-ice feedbacks. Our focus is on the mechanisms that come into play when using similar external forcing with varying amplitudes to induce changes in the tropical Pacific mean state that may influence ENSO.

[11] The orbital parameter changes result in a spatiotemporal redistribution of solar radiation at the top of the atmosphere. A decrease in the obliquity (reduced tilt of the Earth's axis) causes the annual mean insolation to decrease (increase) at high (low) latitudes. The precession, describing the location of the vernal equinox along the Earth's orbit around the Sun, has an influence on the expression of the seasonal cycle in both hemispheres. For example, in the present-day climate, which is close to a precessional extreme, Northern Hemisphere winters are near perihelion, such that today the Northern (Southern) Hemisphere experiences a damped (enhanced) seasonal contrast. Within a distance of half a precessional cycle (~10 kyrs) this pattern is reversed, and in between there is less contrast in the seasonal amplitudes of both the Northern and Southern Hemisphere. High eccentricity, meaning a strongly elliptical orbit further amplifies this pattern of seasonal and hemispheric contrasts.

[12] All simulations were initialized with the World Ocean Atlas (WOA) climatology [*Conkright et al.*, 2002] of temperature and salinity and integrated for 1000 years under constant preindustrial greenhouse gas concentrations (e.g., CO_2: 286 ppmv) [*Petit et al.*, 1999]. The last 500 years of each experiment provide stable climate conditions in the upper ocean and were used for the analyses shown below. All variables were linearly de-trended to remove the remaining small model drift. Monthly climatologies and monthly deseasonalized anomalies were then calculated for selected variables. Finally, the variables were averaged over key regions such as the Niño3 (150°W–90°W, 5°S–5°N) and Niño4 (160°E–150°W, 5°S–5°N) boxes to obtain the mean state and the ENSO indices.

3. Results

3.1. Tropical Pacific Climate in the Preindustrial Control Simulation

[13] To assess the baseline model configuration for the present study, the SSTs from the preindustrial control simulation (0K) are compared with observed SSTs from the Hadley Centre Sea Ice data, HadISST [*Rayner et al.*, 2003] over the period of 1950–1999 (Figures 2a and 2b). The simulated annual mean Equatorial Pacific SSTs (averaged over 120°E–80°W, 5°N–5°S) are about 2°C colder compared to the data (Figures 2a and 2b and Table 2). This is a common bias of non-flux corrected climate models, and possibly due to overly strong trade winds [*Guilyardi*, 2006] and/or too strong vertical mixing in the ocean. The transient climate response (TCR), the temperature change at the time of CO_2 doubling, is 2.9°C in the KCM, which is stronger than in other CMIP3 models (1.2°C–2.6°C) [*Park et al.*, 2009].

[14] The ENSO amplitude in the KCM, defined as the standard deviation of the SST anomalies (SSTA) in the Niño3 region, amounts to 0.91°C, which agrees well with the data (Table 2). However, the small kurtosis and skewness indicate that the Niño3 SSTA distribution is too broad and too symmetric. In particular, the model underestimates the observed tendency towards very strong warm SST anomalies, as indicated by the much larger positive skewness in the Hadley Centre's SST data (Table 2). The spectrum of the Niño3 SST anomalies peaks between 3–4 years, which is slightly shorter than that in the observations (Figure 3). In spite of these differences, which in part may result from the different record length (500 years versus 50 years), the preindustrial control simulation represents the important aspects of the mean Tropical Pacific climate and of ENSO reasonably well.

3.2. Semi-annual and Annual Cycles

[15] The changing orbital configurations during both the Holocene and the Eemian result in an annual mean increase in the top of the atmosphere (TOA) insolation over the Tropics over time due to the decreasing obliquity (Table 1). The annual mean SSTs averaged over the Equatorial Pacific (120°E–80°W, 5°N–5°S) largely follow the obliquity forcing [*Liu et al.*, 2003; *Timmermann et al.*, 2007] with a minor warming trend (~0.1°C) during the early and a considerably stronger warming trend (~0.5°C–0.7°C) during the late

Table 1. Orbital Parameters and Resulting Insolation Forcing Averaged Over the Tropical Pacific (120°E–80°W, 5°N–5°S) for the Different Experiments

	Time Period					
	0K	6K	9.5K	115K	122K	126K
Experiment Name	H0K	H6K	H9K	E15	E22	E26
Eccentricity (deg)	0.0167	0.0187	0.0194	0.0414	0.0407	0.0397
Obliquity (deg)	23.4	24.1	24.2	22.4	23.2	23.9
Precession (ω-180°)	102	1	303	111	356	291
TOA Insolation (Wm^{-2})	416.8	415.9	415.7	418.6	417.5	416.4

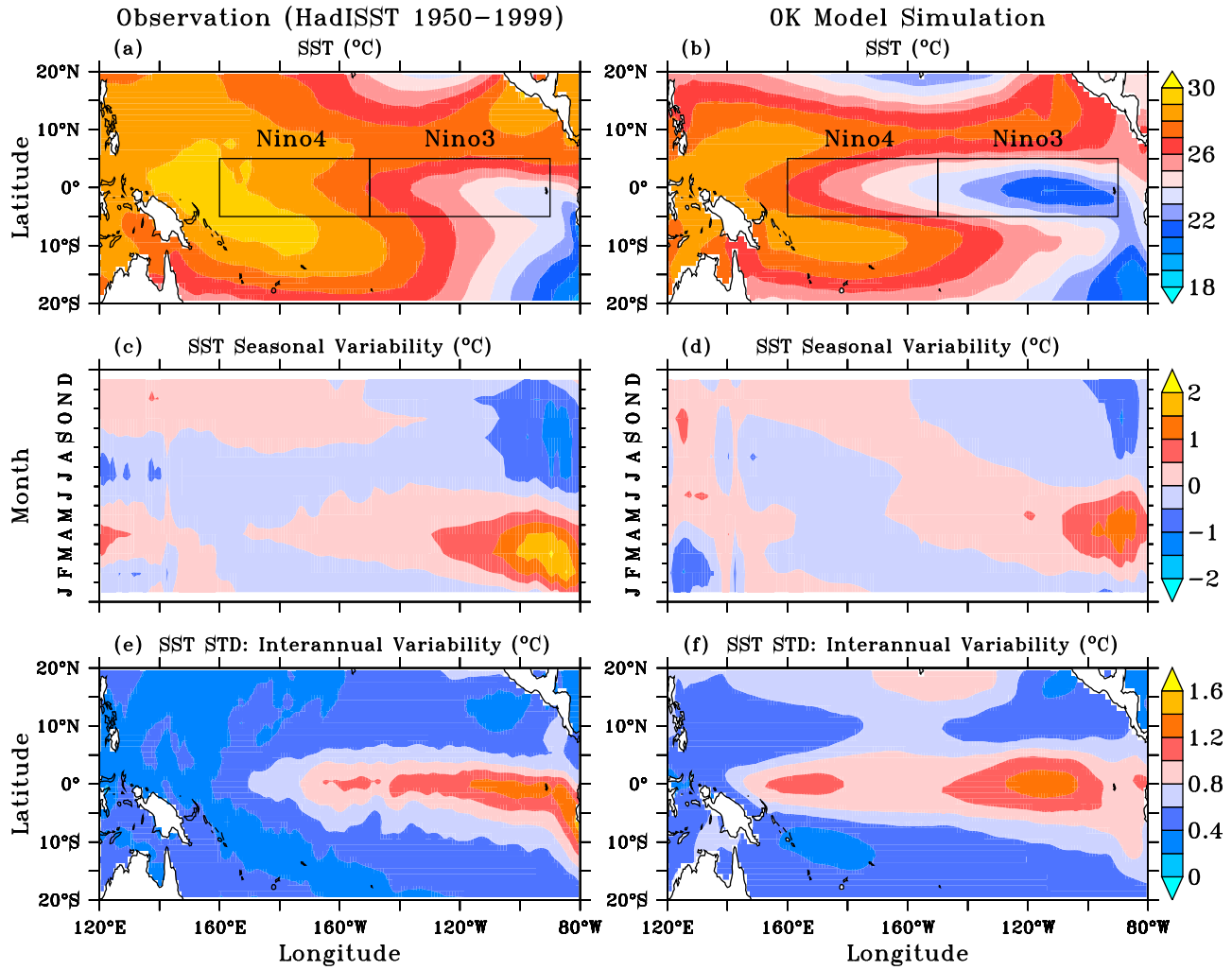

Figure 2. Spatiotemporal variability of SST (°C) in the tropical Pacific (120°E–80°W, 20°N–20°S) from observations (HadISST, 1950–1999; Figures 2a, 2c, and 2e) and the preindustrial control simulation (0K; Figures 2b, 2d, and 2f): (a and b) map of annual mean SST, (c and d) Hovmöller diagram of seasonal SST anomalies, and (e and f) map of standard deviations of the monthly deseasonalized SST anomalies.

phases of both epochs, respectively. Furthermore, there is a precession-induced shift in the semi-annual insolation cycle, which has its insolation maximum in boreal fall (September–October) from the beginning to the middle of both periods, shifting toward boreal spring (March–April) in the late Holocene and Eemian, respectively (Figure 4a).

[16] The semi-annual cycle of the tropical insolation forcing translates into a semi-annual cycle of SST in the WPWP (Figure 4b) with a phase-lag of 1–2 months in all

Table 2. Mean State, SST, Changes of the Tropical Pacific (120°E–80°W, 5°N–5°S) and ENSO Statistics for the Different Experiments and Modern Observations, Hadley SST Data[a]

	Time Period						
	0K	6K	9.5K	115K	122K	126K	HadISST (1950–1999)
Mean SST[b]	25.14	24.62	24.57	25.55	24.91	24.76	27.27
Niño4 SST (°C)	25.69 ± 0.03	25.07 ± 0.03	24.91 ± 0.02	26.15 ± 0.02	25.34 ± 0.03	25.02 ± 0.02	28.44 ± 0.09
Niño3 SST (°C)	22.99 ± 0.02	22.49 ± 0.02	22.54 ± 0.02	23.40 ± 0.02	22.78 ± 0.02	22.81 ± 0.02	25.65 ± 0.09
SST Gradient (°C)	2.70 ± 0.01	2.58 ± 0.01	2.37 ± 0.01	2.75 ± 0.01	2.56 ± 0.01	2.21 ± 0.01	2.79 ± 0.05
ENSO Amplitude (°C)	0.91 ± 0.03	0.86 ± 0.02	0.81 ± 0.03	0.94 ± 0.03	0.84 ± 0.02	0.77 ± 0.03	0.89 ± 0.08
Excess Kurtosis[c]	0.10	−0.07	0.03	0.09	0.41	0.20	1.31
Skewness	0.12	0.04	0.11	0.02	0.11	0.04	0.88

[a]Errors indicate 1 standard error for the data binned into 50-year blocks.
[b]Averaged over 120°E–80°W, 5°N–5°S.
[c]Excess Kurtosis is kurtosis - 3; where 3 is the kurtosis for standard normal distribution. The definition is used so that the standard normal distribution will have an excess kurtosis of zero.

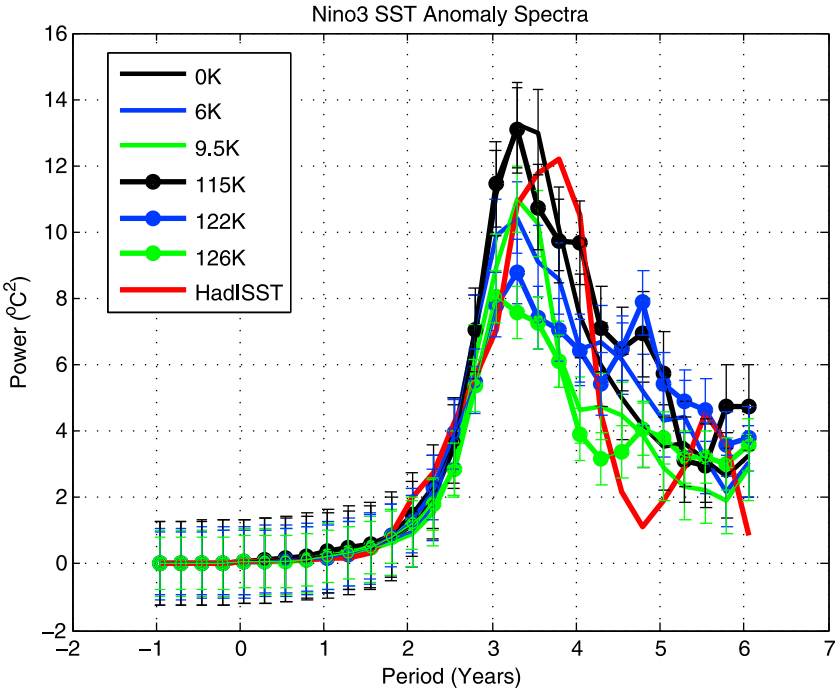

Figure 3. Spectra of monthly deseasonalized Niño3 SST anomalies. The Holocene simulations are shown by the full lines, while the Eemian is marked by circles. Colors indicate the respective early (green; 9.5K, 126K), middle (blue; 6K, 122K), and late (black; 0K, 115K) phases; the red line marks the HadISST data. The error bars (twice the standard error) are overlapping among the time slices, indicating that the changes in ENSO frequencies over the time slices are not statistically significant.

simulations. In the Eastern Equatorial Pacific (Niño3 region), the same forcing results in an annual SST cycle in the late Holocene and late Eemian runs (Figure 4c) presumably due to strong ocean-atmosphere interactions [see, e.g., *Neelin et al.*, 1994; *Philander*, 1999]. An indicator for increasing coupling strength is given by the linear fit of the Niño4 zonal wind stress anomalies against the Niño3 SST anomalies [*Guilyardi*, 2006], where a slight increase of the regression slope over both time periods (Holocene and Eemian) suggests a stronger air-sea coupling (not shown). It is not clear whether the lack of a clear seasonal cycle in the Niño3 region during the other time slices is a model artifact due to too weak air-sea coupling or constitutes a real signal, since paleodata resolving the seasonal cycle are missing.

3.3. Change in ENSO Variability

[17] The periodicity of the Niño3 SST anomalies varies only slightly among the time slice simulations, keeping the peak within the 3–4 year period band (Figure 3). Also higher statistical moments such as skewness and kurtosis exhibit only minor variations among the different simulations (Table 2). However, the ENSO amplitude increases with time during both periods (Holocene, Eemian), with a larger range of amplitudes in the Eemian simulations (Table 2). According to a Student's t-test using 50-year chunks, the changes between the respective early and late phases (Holocene and Eemian) are statistically significant at the 95% level. Consequently, a clear trend toward increasing amplitudes over the course of the Holocene and the Eemian is simulated. This trend is in agreement with observations from the oxygen isotopic δ^{18}O composition of coralline aragonite from Papua New Guinea, which show higher amplitude variability in 118 kyr BP (std 0.08 permil) compared to 128 kyr BP (0.05 permil) [*Tudhope et al.*, 2001]. We are not aware of any other robust paleodata for the Eemian ENSO, but our result is also in good agreement with Holocene proxy data, as described above.

[18] The ENSO amplitude and the Tropical Pacific mean state depict a clear linear behavior: the ENSO amplitude increases (1) with the annual mean SST averaged over both the Niño3 and Niño4 regions (Figure 5a), (2) with an increased west-east (Niño4 minus Niño3) SST gradient (Figure 5b), and (3) with an enhanced amplitude of the seasonal SST cycle in the Niño3-box (Figure 5b). As expected from *Guilyardi* [2006], the ENSO amplitude increases with reduced easterly wind stress in the Niño4-box (Figure 5c) and with increased easterly wind stress in the Niño3-box. However, there is no clear relationship with the Equatorial Pacific upper ocean heat content, as expressed by the depth of the 20°C-isotherm (Figure 5d). This indicates that in our simulations, the ENSO amplitude changes mostly originate from surface layer processes. This is in accordance with *Guilyardi* [2006], where most of the reported models were locked in the surface (SST-) mode [*Neelin et al.*, 1998].

[19] Overall, the SST in the Equatorial Pacific seems to be a key parameter controlling ENSO amplitude in the KCM (Figure 5a). In particular, the strong correlation between the ENSO amplitude and the Niño4 SST (r = 0.89) suggests that the WPWP region is a suitable area to reconstruct ENSO strength during the past. One reason for the higher SST sensitivity to orbital forcing in the Western Equatorial Pacific relative to the EEP is that in the latter the insolation-

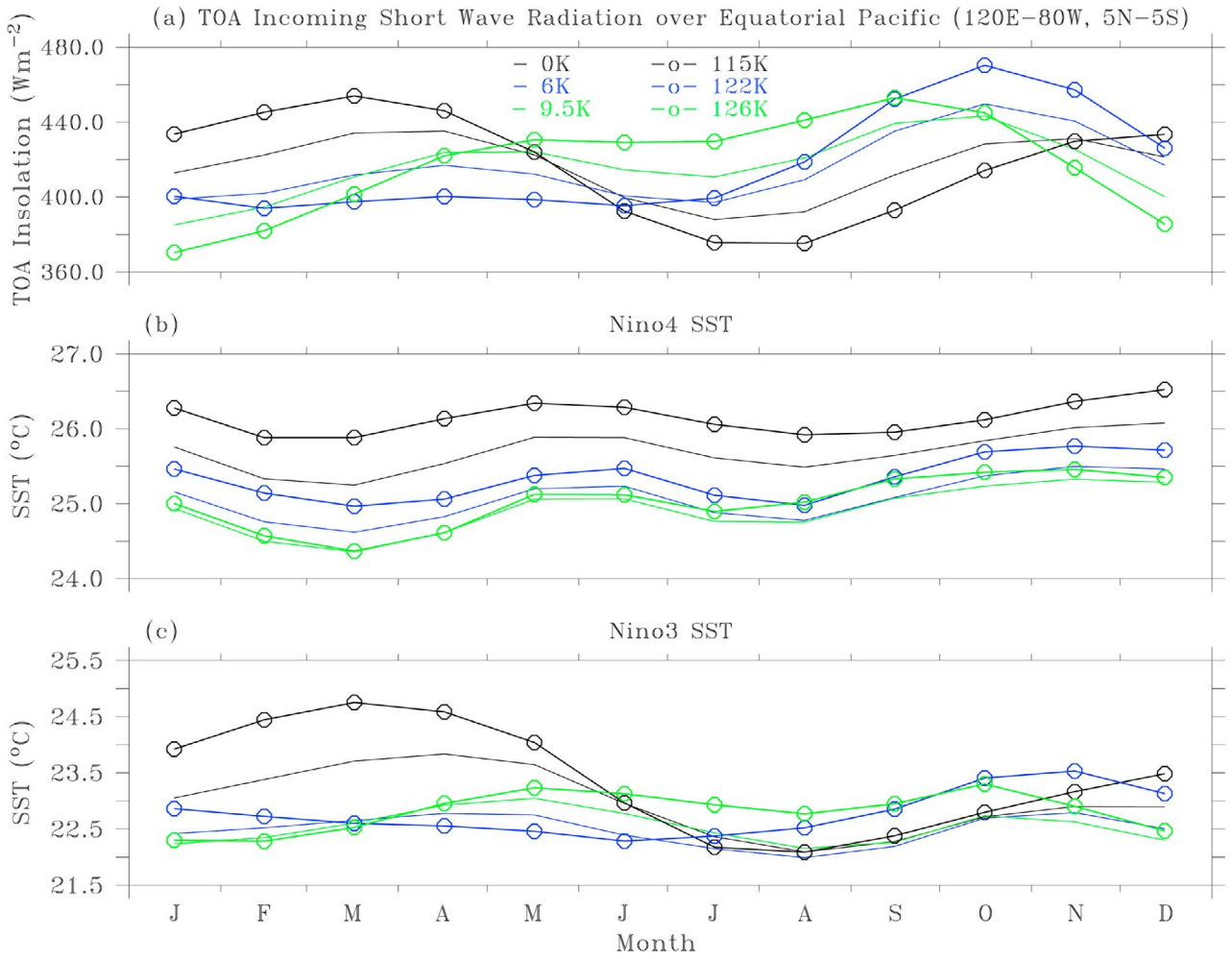

Figure 4. Monthly averages over the Equatorial Pacific (120°E–80°W, 5°N–5°S) of (a) top of atmosphere (TOA) incoming short wave radiation (Wm^{-2}), (b) Niño4 SST (°C), and (c) Niño3 SST (°C). Line and color code as in Figure 3.

induced warming is damped by increased upwelling [*Liu*, 1998]. As a consequence, the zonal west-east SST gradient increases with time over both the Holocene and the Eemian, and this yields an even higher correlation with the ENSO amplitude (r = 0.97) than the Niño4 SST only (Figures 5a and 5b).

3.4. Walker Circulation

[20] The strengthening of the west-east SST gradient over time is further investigated through the simulated changes in the atmospheric circulation. The wind stress response pattern during the Holocene (0K minus 9.5K; Figure 6a) and the Eemian (115K minus 126K; Figure 6b) indicates a strong meridional (Ekman) convergence of warm surface waters in the western half of the upper Equatorial Pacific. The low-level velocity potential simulated in 0K is shown in Figure 7a, depicting, as expected, a strong convergence of air masses in the WPWP region as indicated by the strong maximum there. In contrast, the EEP features a divergence of air masses. Differences of the velocity potential during the Holocene (0K–9.5K; Figure 7c color shading) and the Eemian (115K–126K; Figure 7e color shading) are consistent with the corresponding SST changes shown in Figures 6a and 6b, respectively. The changes in the velocity potential include an anomalous convergence in the Central Pacific peaking at about 160°W in both cases (Figures 7c and 7e color shading). The changes in SST and velocity potential are stronger during the Eemian (Figures 6b and 7e) compared to those during the Holocene (Figures 6a and 7c). This is due to the pronounced influence of the higher eccentricity during the Eemian on the strength of the precession forcing, whereas the spatial response patterns remain very similar. The anomalous convergence in the Central Pacific is mainly due to an eastward expansion of the WPWP in both 0K and 115K (Figures 7c and 7e; black contours), very much as during El Niño events.

[21] The associated zonal (Walker) circulation changes are shown as averages over the equatorial region (10°S–10°N). They depict in 0K the familiar pattern with upward motion over the WPWP centered at about 130°E and subsidence further to the east (Figure 7b). The estimate of the Walker circulation strength (based on the maximum value of the velocity potential over the western Pacific) does not show strong changes from the early to the late Holocene (Eemian)

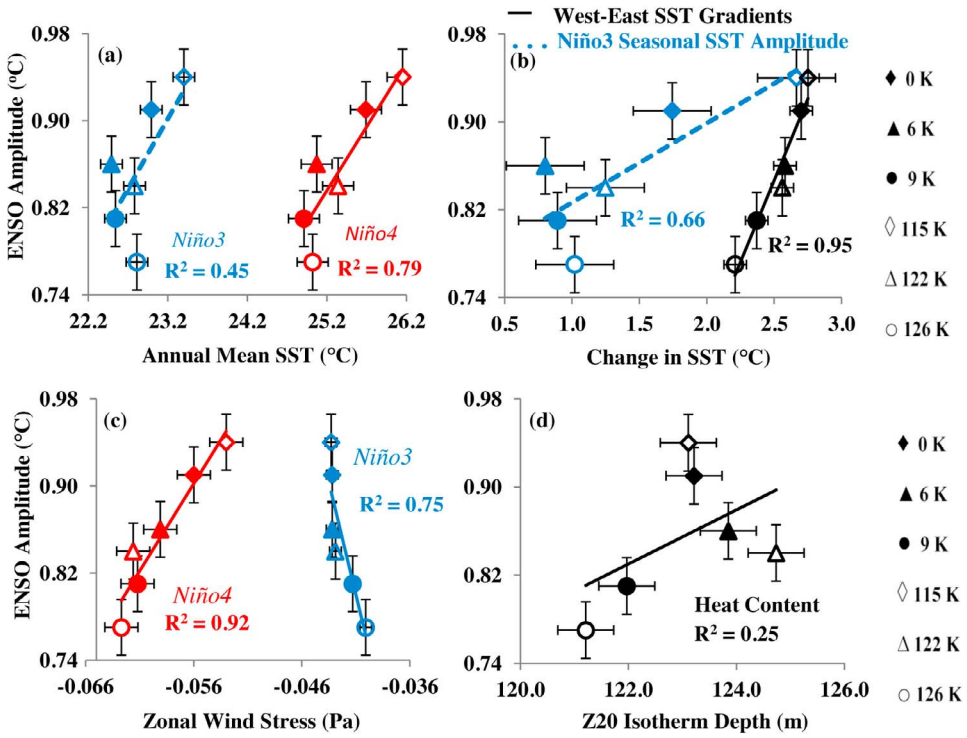

Figure 5. Relationships between the ENSO amplitude (°C) and (a) the annual mean Niño3 (blue) and Niño4 (red) SSTs, (b) SST zonal gradient (Niño4-Niño3; black) and Niño3 SST seasonal amplitude (maximum – minimum Niño3 SST; blue), (c) Niño3 (blue) and Niño4 (red) zonal wind stress, and (d) averaged Niño3 and Niño4 20°C isotherm (Z20) depth, respectively. The error bars correspond to 1 standard error using ten 50-year bins. Please note that the easterly wind stress is stronger as it becomes more negative.

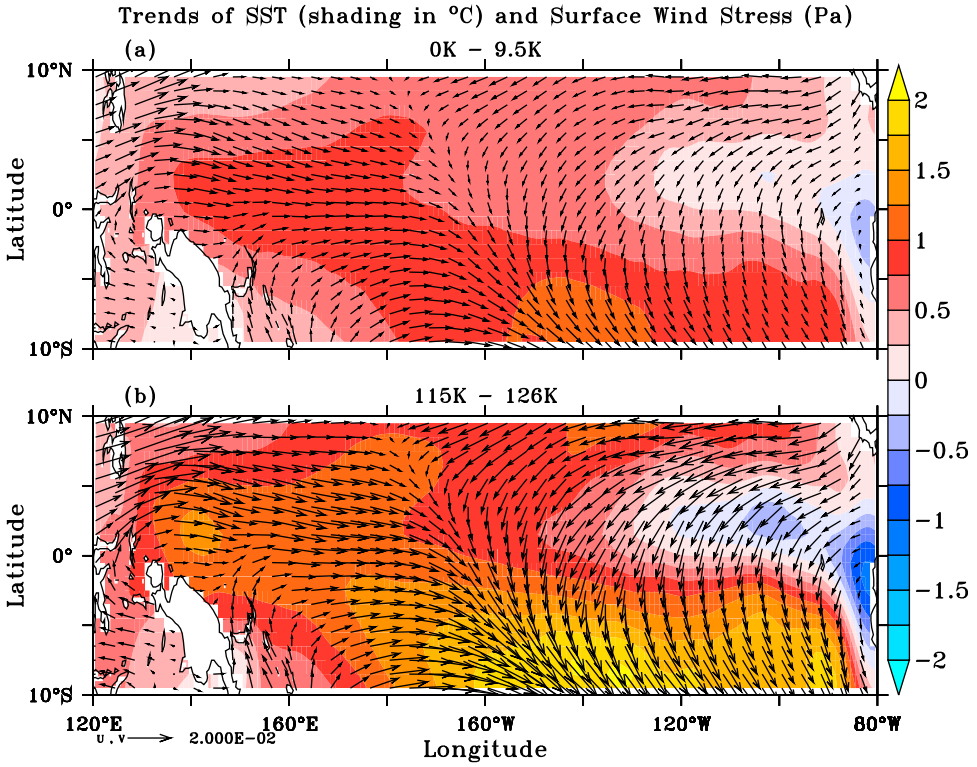

Figure 6. Difference of SST (°C) (shading) and surface wind stress (Pa) between two periods in (a) the Holocene (0K minus 9.5K) and (b) the Eemian (115K minus 126K).

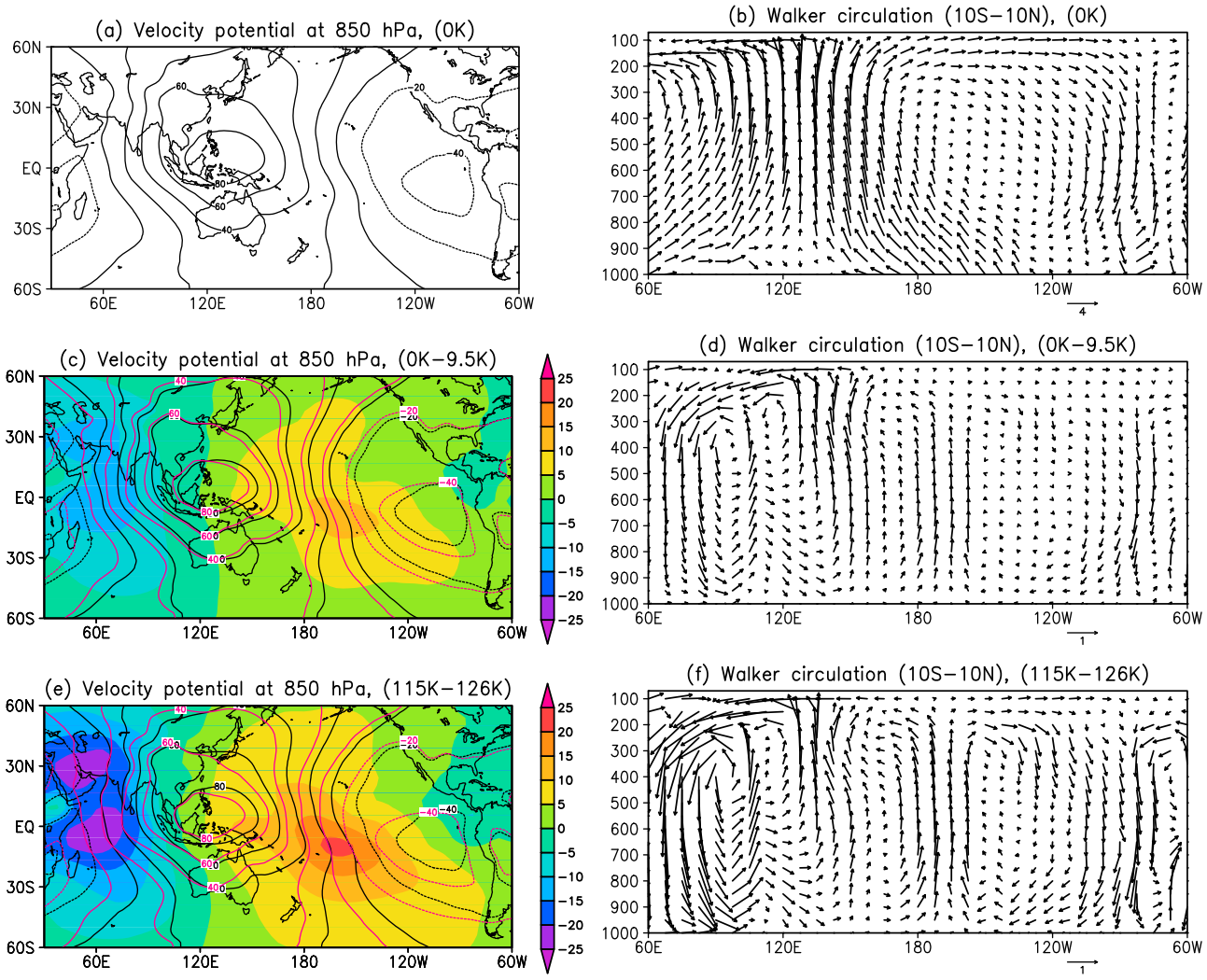

Figure 7. (a) Annual mean 850 hPa velocity potential (10^6 m^2s^{-1}) and (b) zonal-vertical circulation for the preindustrial simulation (0K). The zonal-vertical circulation is shown by averaging divergent wind (m s^{-1}) and vertical velocity (10^{-4} hPa s^{-1}) between 10°S and 10°N. (c) Holocene trend (0K minus 9.5K; shaded) of the mean 850 hPa velocity potential, overlaid by the annual mean contours of the preindustrial (0K; black) and early Holocene (9.5K; red) and (d) that of the zonal-vertical circulation. (e) Eemian trend (115K minus 126K; shaded) of the mean 850 hPa velocity potential, overlaid by the contours of the late Eemian (115K; black) and early Eemian (126K; red) and (f) that of the zonal-vertical circulation.

(Figures 7c and 7e). However, there is a substantial eastward shift of the area of strong upward motion (seen as anomalous upward motion in Figures 7d and 7f), which is indicated by the shift of the zero-contours in Figures 7c and 7e. This implies a reduction of the easterlies in the Western Pacific and a corresponding strengthening in the Eastern Pacific (Figures 7d and 7f), while the total strength of the Walker circulation remains rather constant, exhibiting changes of less than 5%.

3.5. Changes in the Surface Heat Flux and Ocean Heat Transport

[22] Differences in the net surface heat flux between the respective early and late stages of both warm periods (Holocene, Eemian) reveal anomalous cooling over the warm pool and anomalous warming in the east (Figures 8a and 8b). This suggests that the surface heat flux cannot explain the stronger warming in the west compared to the east, but rather represents a damping. This implies that the cause of the warming in the west during the two warm epochs must be explained by ocean dynamical processes. Following *DiNezio et al.* [2009], we investigate the contributions of the vertically integrated meridional (Qv), vertical (Qw) and zonal (Qu) ocean dynamical heating contributions in the upper 300 m (H) using:

$$Qv = \rho c \int_{-H}^{0} v \frac{\partial T}{\partial y} dz, \tag{1}$$

$$Qw = \rho c \int_{-H}^{0} w \frac{\partial T}{\partial z} dz, \tag{2}$$

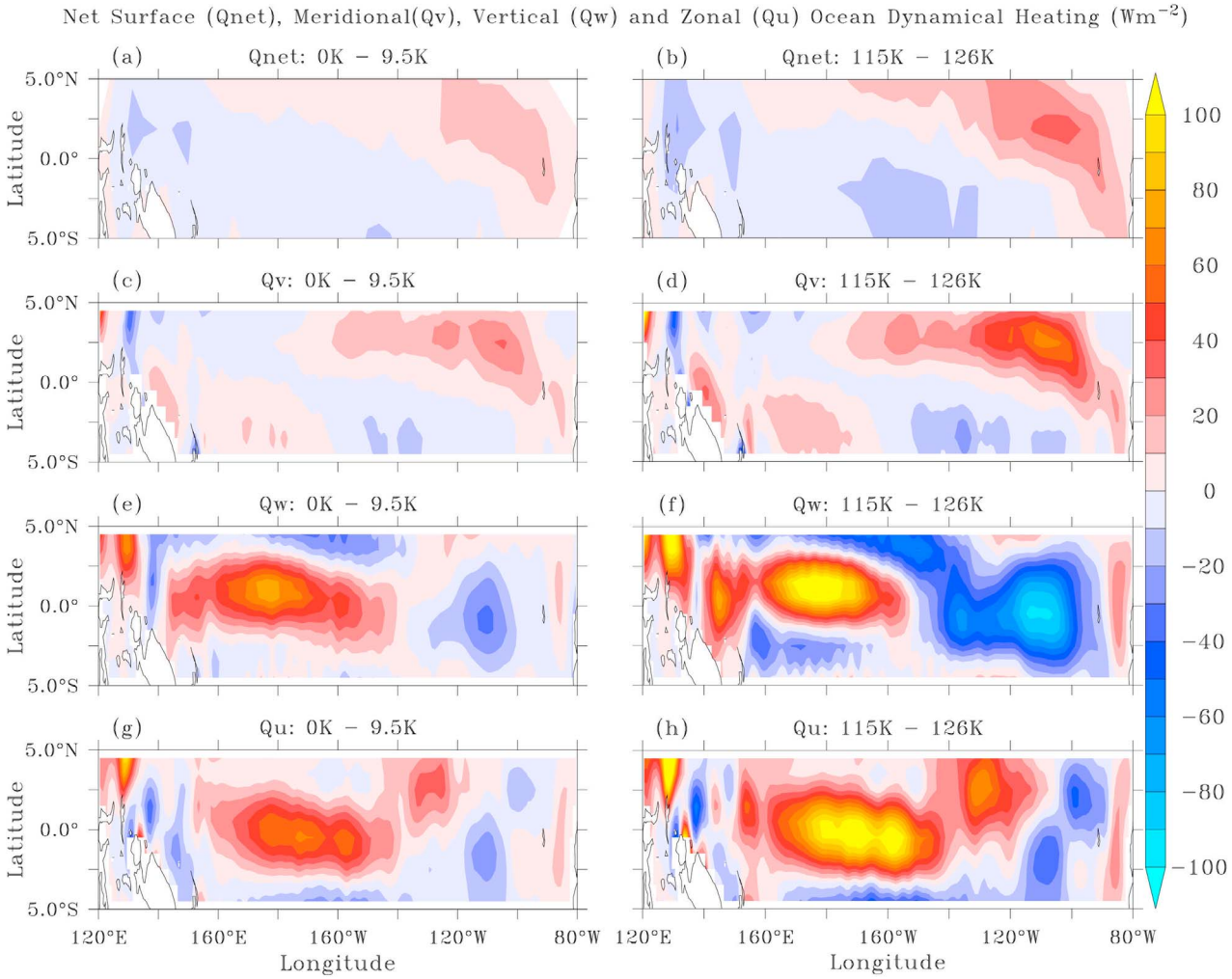

Figure 8. Holocene (Figures 8a, 8c, 8e, and 8g) and Eemian (Figures 8b, 8d, 8f, and 8h) trends of the (a and b) net surface heat flux (Q_{net}), (c and d) meridional (Q_v), (e and f) vertical (Q_w), and (g and h) zonal (Qu) ocean dynamical heating (Wm^{-2}) over water in the tropical Pacific. Positive values are directed into the ocean.

$$Qu = \rho c \int_{-H}^{0} u \frac{\partial T}{\partial x} dz, \tag{3}$$

where $\rho c = 4.1 \times 10^6$ Jm^{-3} K^{-1}, c the specific heat capacity of water, and ρ the density of water.

[23] The spatial patterns of the net surface heat flux (Figures 8a and 8b) and Qv (Figures 8c and 8d) are similar and do not depict strong changes along the Equator. Thus both cannot explain the enhanced equatorial zonal temperature gradient change. The term Qw shows stronger ocean dynamical cooling through vertical advection in the EEP and a warming tendency to the west in 0K (115K) when compared to 9.5K (126K) (Figures 8e and 8f). Further, the distribution of Qu is similar to that of Qw (Figures 8g and 8h). We can therefore conclude that it is the zonal heat advection (Qu) in concert with the vertical heat advection (Qw) that cause the west-east asymmetry in the SST-trends during the two warm periods. The effect is stronger during the Eemian compared to the Holocene, which is consistent with the stronger insolation forcing during the Eemian.

[24] In order to investigate the changes in the upper ocean in more detail, we analyzed the temperature and vertical velocity structure in the vertical plane parallel to the Equator (Figure 9). Figures 9a and 9b show the mean temperature in the x–z section along the Equator for 0K and 115K, respectively. Figures 9c and 9d depict the temperature anomalies (0K minus 9.5K and 115K minus 126K, respectively). No clear signal in the thermocline structure along the Equator is found. However, the vertical velocity shown in Figures 9e and 9f displays a clear pattern, with enhanced vertical velocity in the east and reduced vertical velocity in the west. This supports the development of an enhanced equatorial zonal SST gradient. The major contribution to the latter is from the west, where the temperature increase is on the order of 1°C, whereas the surface ocean warms considerably less to the east.

[25] We conclude that the increase in the WPWP SST is the main reason for the stronger ENSO variability, because

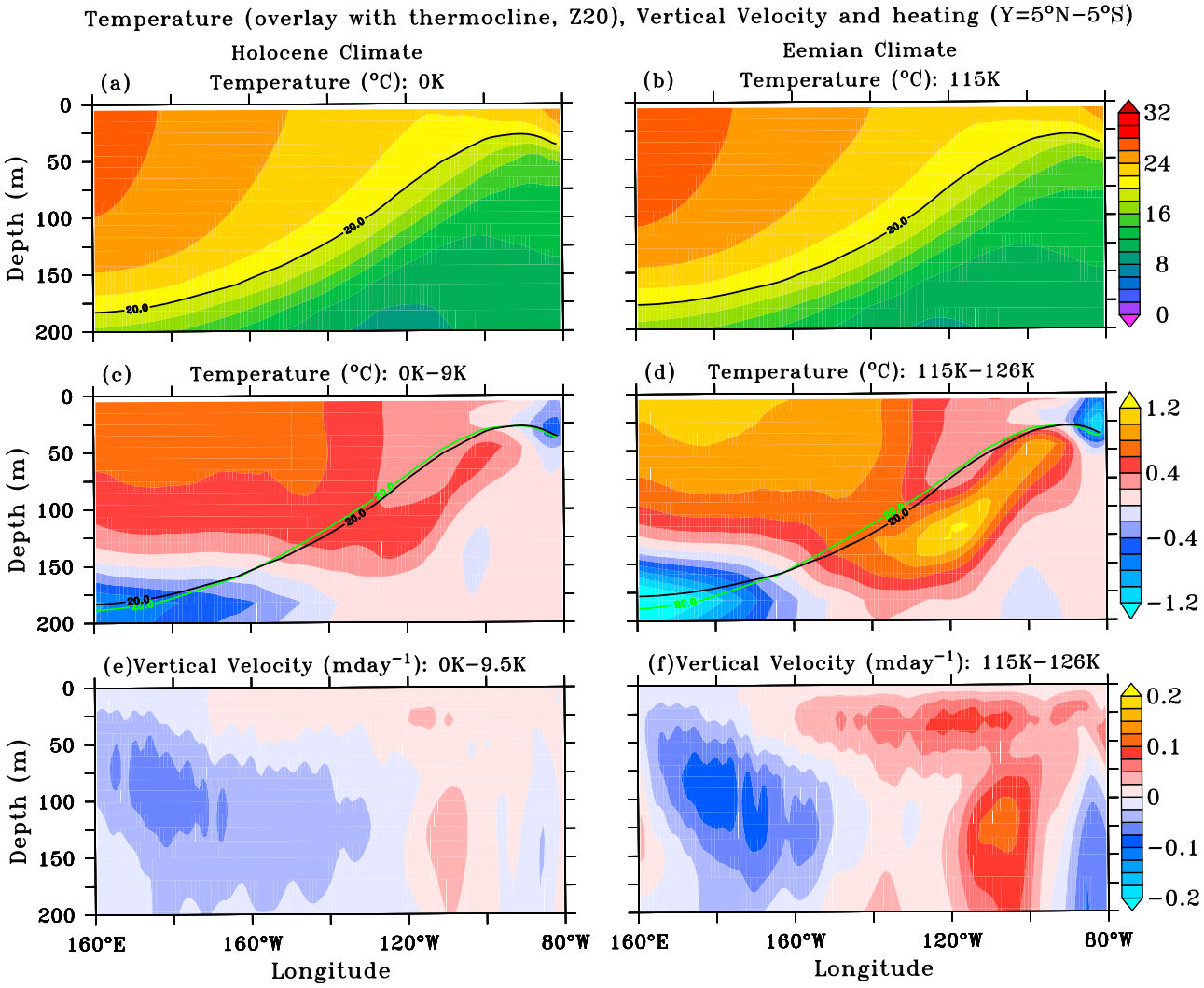

Figure 9. Holocene (Figures 9a, 9c, and 9e) and Eemian (Figures 9b, 9d, and 9f) depth-longitude variations in the (a and b) mean temperature (0K, 115K), (c and d) the trends of the temperature overlain with the thermocline (Z20) depths, and (e and f) trends of vertical velocity with positive values indicating upward anomalies. The Z20 lines with green and black colors represent the early and late Holocene (Eemian), respectively.

the diabatic heating in this region is strongly dependent on the mean SST [*Zebiak and Cane*, 1987]. For instance, the regression of Niño4 zonal wind stress anomalies on Niño3 SST anomalies amounts to about 0.0053 Pa°C^{-1} in 115K, while it is reduced to 0.0047 Pa°C^{-1} in 126K (not shown). This indicates a stronger wind stress sensitivity to SST anomalies with higher mean temperatures. The corresponding change in SST variability between the two time slices as expressed by the standard deviation of the Niño3 SST anomalies is of the order of 20% (see Table 2). Although the change in the wind stress sensitivity cannot account for the all change in ENSO variability, it is obviously a major contributor.

4. Discussion

[26] Our climate model simulations have shown that the ENSO amplitude does increase with an overall warming of the Tropical Pacific as a result of orbitally induced insolation changes. The ENSO amplitude also increases with a higher west-east equatorial SST gradient and with an enhanced seasonal cycle of the SSTs in the EEP. The ENSO frequency remains largely unchanged. Variations in orbital forcing have been identified as the main driver of climate variability during the Holocene [*Lorenz et al.*, 2006; *Braconnot et al.*, 2008; *Berger*, 1988], and they were also important factors driving climate change during the Eemian [*Montoya et al.*, 2000; *Kutzbach et al.*, 1991; *Crowley and Kim*, 1994]. Both model studies [*Zheng et al.*, 2008; *Timmermann et al.*, 2007] and paleoreconstructions [*Tudhope et al.*, 2001] have previously linked changes in ENSO to variations in the seasonal distribution of solar radiation through fluctuations in the precessional cycle. When relating the simulated reorganizations of SST and ENSO amplitude in the Tropical Pacific to the individual forcing components (obliquity, precession), we find that the overall warming of the Tropical Pacific can be well explained by the decreasing obliquity, while the ENSO amplitude is most sensitive to precessional forcing (Figure 10). In the WPWP, however, the warming is also

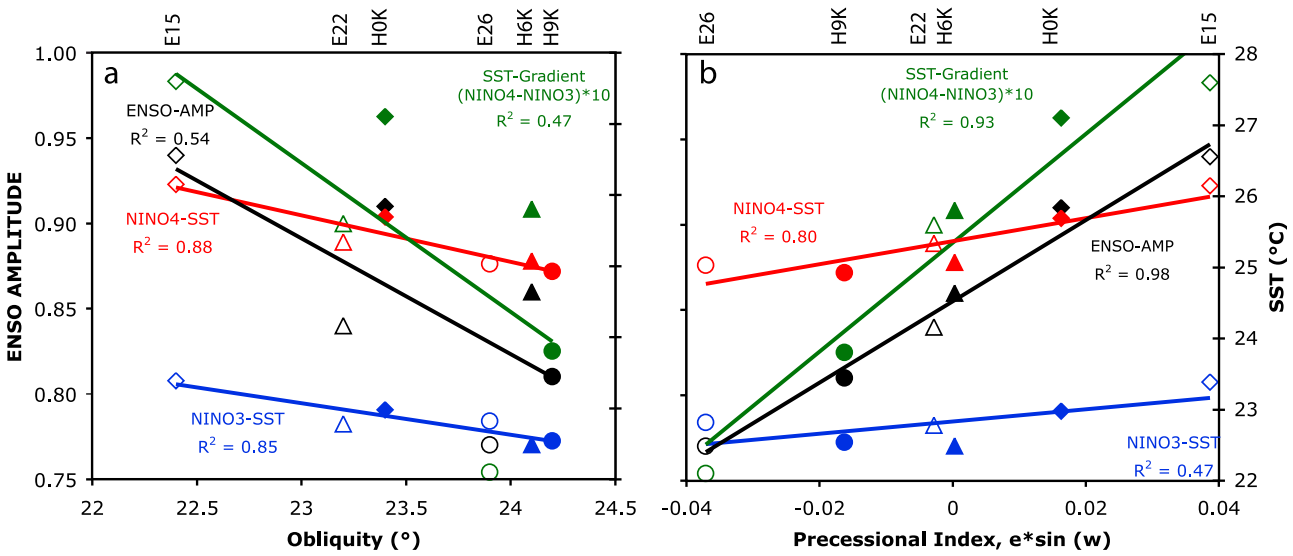

Figure 10. Changes in the characteristics of the tropical Pacific mean state and ENSO versus the individual forcing components: (a) obliquity and (b) precession; ENSO amplitude (black; left scale), Niño4 SST (red; right scale), Niño3 SST (blue; right scale). Note that the west-east SST gradient (green; right scale) is multiplied by 10 times to match the scale.

strongly correlated to changes in the precessional index. Ocean dynamical processes, however, play the key role for the enhanced warming in the west.

[27] The simulated mean temperature trend largely agrees with alkenone reconstructions that show a tropical warming over the Holocene [*Kim et al.*, 2004; *Leduc et al.*, 2010; *Schneider et al.*, 2010], which is also confirmed by other climate models [*Voss and Mikolajewicz*, 2001; *Lorenz and Lohmann*, 2004; *Lorenz et al.*, 2006]. An enhancing ENSO amplitude was also reconstructed over the Holocene from a large number of paleoproxies [*Rodbell et al.*, 1999; *Tudhope et al.*, 2001; *Moy et al.*, 2002; *Gagan et al.*, 2004] and simulated by other climate models [*Zheng et al.*, 2008]. In contrast to model simulations of *Timmermann et al.* [2007] and *Liu* [2002], where the ENSO amplitude increases as the seasonal cycle weakens due to frequency entrainment, our model results show a combined increase of both seasonal and ENSO amplitude. Furthermore, we do not find a positive linear relationship between the ENSO amplitude and the seasonal phase lock index (amplitude of the monthly stratified standard deviation of Niño3 SST anomaly) as reported by *Guilyardi* [2006] and *Zheng et al.* [2008]. This can be explained by the failure of the KCM to capture the strong phase locking of the ENSO to the annual cycle [see also *Park et al.*, 2009].

[28] Overall, the amplified warming of the Western Pacific leads to a larger atmospheric heating there compared to the east, where deep convection is suppressed in response to a cooling feedback from the shallow thermocline and enhanced upwelling. The enhanced west-east equatorial SST gradient represents a more La Niña-like mean state of the tropical Pacific in an orbital warm Northern Hemisphere (NH) summer as stated by *Clement et al.* [1999]. Consequently, in a cooler NH summer the mean state can be expected to be more El Niño-Like, which may also be linked to a weak Asian summer monsoon over the tropical Pacific (not shown) [see also *Liu et al.*, 2000, and references therein]. These results are also consistent with findings from CO_2-induced global warming scenarios as reported by *Meehl et al.* [2001] and *Collins et al.* [2010], who both linked an increase in ENSO amplitude to a higher west-east SST gradient. However, it should be noted that the CO_2 warming scenario can differ from orbital forcing, since the former is a globally uniform forcing all year-round, while the latter varies with latitude and is more confined to the seasonal cycle signal. In addition, our results are in agreement with the multimodel ensemble reported by *Guilyardi* [2006], where an inverse relationship is found between the ENSO amplitude and the Niño4 mean zonal wind stress. Overall, our findings on the link between the ENSO amplitude and the mean Tropical Pacific SSTs agree well with previous studies, and we argue that especially the warming in the Western Equatorial Pacific is the key factor controlling the simulated changes in the ENSO amplitude.

[29] We find that a precession-induced southward shift of the Intertropical Convergence Zone (ITCZ) in 0K (115K) over the Equatorial Pacific is accompanied by a reduction of the annual mean meridional gradient of SST (12°N–5°N minus 12°S–5°S) [see also *Timmermann et al.*, 2007]. The corresponding changes in the meridional SST gradients are stronger in the Eastern Pacific compared to the values over the entire Equatorial Pacific. This is due to the more northward position of the ITCZ in the east, favoring an intensification of cross equatorial southerlies over the EEP and increased upwelling. The southward migration of the mean northern position of the ITCZ is further supported by the reduced warming in the Northern Hemisphere in 0K and 115K, where boreal summer occurs at aphelion. This is in agreement with *Koutavas et al.* [2006] who concluded from Mg/Ca thermometry near the Galapagos Islands that a more

southward displaced ITCZ in the late Holocene would favor higher El Niño-like instability.

5. Conclusions

[30] We used a climate model to investigate the sensitivity of El Niño–Southern Oscillation (ENSO) to changes in the mean climate state, induced by variations in the orbital parameters (eccentricity obliquity, and precession), resembling the past interglacial periods of the Holocene (last 10 kyr) and the Eemian (126–115 kyr BP). The simulated ENSO amplitude increases linearly with sea surface temperatures (SSTs) in the Tropical Pacific and with an increased west-east equatorial SST gradient. The higher damping of the SST changes in the Eastern Pacific compared to the Western Pacific is largely induced by fluctuations in the vertical ocean dynamical heating with contribution from the zonal heat transport. At the same time, the ENSO frequencies remain rather constant within a broad range peaking at periods of 3–4 years, which is close to modern observations. Our results provide important insights into the mechanisms that are controlling ENSO variability and they are in fairly good agreement with paleoreconstructions and other climate model simulations for the Holocene. According to our findings, the Western Pacific Warm Pool (WPWP) SST is a suitable indicator of past ENSO variability. The robust link to the mean climate state in the Tropical Pacific provides a powerful tool to be tested by paleoreconstructions that only allow resolution of the mean state, but which do not resolve higher frequency internal climate variability. We propose that it may also be used in future climate projections that are usually assumed to be more reliably predicting the mean state rather than interannual variability.

[31] **Acknowledgments.** This work was supported by the Cluster of Excellence 'The Future Ocean' (DFG EXC80/1) and the SFB754, funded by the German Science Foundation (DFG). The model integrations were performed at the Computing Centre at Kiel University.

References

Berger, A. L. (1978), Long-term variations of daily insolation and Quaternary climatic changes, *J. Atmos. Sci.*, *35*, 2363–2367.

Berger, A. L. (1988), Milankovitch theory and climate, *Rev. Geophys.*, *26*, 624–657, doi:10.1029/RG026i004p00624.

Blanke, B., J. D. Neelin, and D. Gutzler (1997), Estimating the effect of stochastic wind stress forcing on ENSO irregularity, *J. Clim.*, *10*, 1473–1486, doi:10.1175/1520-0442(1997)010<1473:ETEOSW>2.0.CO;2.

Braconnot, P., C. Marzin, L. Grégoire, E. Mosquet, and O. Marti (2008), Monsoon response to changes in Earth's orbital parameters: Comparisons between simulations of the Eemian and of the Holocene, *Clim. Past*, *4*, 281–294, doi:10.5194/cp-4-281-2008.

Brown, J., M. Collins, and A. Tudhope (2006), Coupled model simulations of mid-Holocene ENSO and comparisons with coral proxy records, *Adv. Geosci.*, *6*, 29–33, doi:10.5194/adgeo-6-29-2006.

Chavez, F. P., P. G. Strutton, G. E. Friederich, R. A. Feely, G. C. Feldman, D. G. Foley, and M. J. McPhaden (1999), Biological and chemical response of the Equatorial Pacific Ocean to the 1997–98 El Niño, *Science*, *286*, 2126–2131, doi:10.1126/science.286.5447.2126.

Clement, A. C., R. Seager, and M. A. Cane (1999), Orbital controls on ENSO and tropical climate, *Paleoceanography*, *14*, 441–456, doi:10.1029/1999PA900013.

Clement, A. C., Seager, R., and M. A. Cane (2000), Suppression of El Niño during the mid-Holocene by changes in the Earth's orbit, *Paleoceanography*, *15*, 731–737, doi:10.1029/1999PA000466.

Collins, M., et al. (2010), The impact of global warming on the tropical Pacific Ocean and El Niño, *Nat. Geosci.*, *3*, 391–397, doi:10.1038/ngeo868.

Conkright, M. E., R. A. Locarnini, H. E. Garcia, D. O'Brien, T. P. Boyer, C. Stephens, and J. I. Antonov (2002), *World Ocean Atlas 2001: Objective Analyses, Data Statistics, and Figures* [CD-ROM], *Natl. Oceanogr. Data Cent. Int. Rep.*, vol. 17, 17 pp., NOAA, Silver Spring, Md.

Crowley, T. J., and K.-Y. Kim (1994), Milankovitch forcing of the last interglacial sea level, *Science*, *265*, 1566–1568, doi:10.1126/science.265.5178.1566.

Dijkstra, H. A., and G. Burgers (2002), Fluid dynamics of El Niño variability, *Annu. Rev. Fluid Mech.*, *34*, 531–558, doi:10.1146/annurev.fluid.34.090501.144936.

DiNezio, P. N., A. C. Clement, G. A. Vecchi, B. J. Soden, B. P. Kirtman, and S.-K. Lee (2009), Climate response of the Equatorial Pacific to global warming, *J. Clim.*, *22*, 4873–4892, doi:10.1175/2009JCLI2982.1.

Eckert, C., and M. Latif (1997), Predictability of a stochastically forced hybrid coupled model of El Niño, *J. Clim.*, *10*, 1488–1504, doi:10.1175/1520-0442(1997)010<1488:POASFH>2.0.CO;2.

Fedorov, A. V., and S. G. Philander (2000), Is El Niño changing?, *Science*, *288*, 1997–2002, doi:10.1126/science.288.5473.1997.

Fichefet, T., and M. A. Morales Maqueda (1997), Sensitivity of a global sea ice model to the treatment of ice thermodynamics and dynamics, *J. Geophys. Res.*, *102*, 12,609–12,646, doi:10.1029/97JC00480.

Gagan, M. K., E. J. Hendy, S. G. Haberle, and W. S. Hantoro (2004), Post-glacial evolution of the Indo-Pacific Warm Pool and El Niño–Southern Oscillation, *Quat. Int.*, *118–119*, 127–143, doi:10.1016/S1040-6182(03)00134-4.

Ganopolski, A., C. Kubatzki, M. Claussen, V. Brovkin, and V. Petoukhov (1998), The influence of vegetation-atmosphere-ocean interaction on climate during the mid-Holocene, *Science*, *280*, 1916–1919, doi:10.1126/science.280.5371.1916.

Guilyardi, E. (2006), El Niño-mean state-seasonal cycle interactions in a multi-model ensemble, *Clim. Dyn.*, *26*, 329–348, doi:10.1007/s00382-005-0084-6.

Guilyardi, E., A. Wittenberg, A. Fedorov, M. Collins, C. Wang, A. Capotondi, G. J. van Oldenborgh, and T. Stockdale (2009), Understanding El Niño in ocean-atmosphere general circulation models: Progress and challenges, *Bull. Am. Meteorol. Soc.*, *90*, 325–340, doi:10.1175/2008BAMS2387.1.

Hays, J. D., J. Imbrie, and N. J. Shackleton (1976), Variations in the Earth's orbit: Pacemaker of the ice ages, *Science*, *194*, 1121–1132, doi:10.1126/science.194.4270.1121.

Intergovernmental Panel on Climate Change (2007), Summary for policymakers, in *Climate Change 2007: The Physical Science Basis: Working Group I Contribution to the Fourth Assessment Report of the Intergovernmental Panel on Climate Change*, edited by S. Solomon et al., pp. 437–505, Cambridge Univ. Press, New York.

Jansen, E., et al. (2007), Palaeoclimate, in *Climate Change 2007: The Physical Science Basis: Working Group I Contribution to the Fourth Assessment Report of the Intergovernmental Panel on Climate Change*, edited by S. Solomon et al., pp. 437–505, Cambridge Univ. Press, New York.

Joussaume, S., and K. E. Taylor (1995), Status of the Paleoclimate Modeling Intercomparison Project (PMIP), in *Proceedings of the First International AMIP Scientific Conference*, *Rep. 92*, pp. 425–430, World Clim. Res. Programme, Geneva, Switzerland.

Kessler, W. S. (2002), Is ENSO a cycle or a series of events?, *Geophys. Res. Lett.*, *29*(23), 2125, doi:10.1029/2002GL015924.

Khon, V., W. Park, M. Latif, I. I. Mokhov, and B. Schneider (2010), Response of the hydrological cycle to orbital and greenhouse gas forcing, *Geophys. Res. Lett.*, *37*, L19705, doi:10.1029/2010GL044377.

Kim, J.-H., N. Rimbu, S. J. Lorenz, G. Lohmann, S.-I. Nam, S. Schouten, C. Rühlemann, and R. R. Schneider (2004), North Pacific and North Atlantic sea-surface temperature variability during the Holocene, *Quat. Sci. Rev.*, *23*, 2141–2154, doi:10.1016/j.quascirev.2004.08.010.

Kleeman, R., and A. M. Moore (1997), A theory for the limitation of ENSO predictability due to stochastic atmospheric transients, *J. Atmos. Sci.*, *54*, 753–767, doi:10.1175/1520-0469(1997)054<0753:ATFTLO>2.0.CO;2.

Koutavas, A., P. B. deMenocal, G. C. Olive, and J. Lynch-Stieglitz (2006), Mid-Holocene El Niño–Southern Oscillation (ENSO) attenuation revealed by individual foraminifera in eastern tropical Pacific sediments, *Geology*, *34*, 993–996, doi:10.1130/G22810A.1.

Kutzbach, J. E., and Z. Liu (1997), Response of the African Monsoon to orbital forcing and ocean feedbacks in the middle Holocene, *Science*, *278*, 440–443, doi:10.1126/science.278.5337.440.

Kutzbach, J. E., R. G. Gallimore, and P. J. Guetter (1991), Sensitivity experiments on the effects of orbitally caused insolation changes on the interglacial climate of high northern latitudes, *Quat. Int.*, *10–12*, 223–229.

Larkin, N. K., and D. E. Harrison (2002), ENSO warm (El Niño) and cold (La Niña) event life cycles: Ocean surface anomaly patterns, their symmetries, asymmetries, and implications, *J. Clim.*, *15*, 1118–1140, doi:10.1175/1520-0442(2002)015<1118:EWENOA>2.0.CO;2.

Lau, K. M. (1985), Elements of a stochastic-dynamical theory of long-term variability of the El Niño-Southern Oscillation, *J. Atmos. Sci.*, *42*, 1552–1558, doi:10.1175/1520-0469(1985)042<1552:EOASDT>2.0.CO;2.

Leduc, G., R. Schneider, J.-H. Kim, and G. Lohmann (2010), Holocene and Eemian Sea surface temperature trends as revealed by alkenone and Mg/Ca paleothermometry, *Quat. Sci. Rev.*, *29*, 989–1004, doi:10.1016/j.quascirev.2010.01.004.

Li, J., S.-P. Xie, E. R. Cook, G. Huang, R. D'Arrigo, F. Liu, J. Ma, and X.-T. Zheng (2011), Interdecadal modulation of El Niño amplitude during the past millennium, *Nat. Clim. Change*, *1*, 114–118, doi:10.1038/nclimate1086.

Liu, Z. (1998), The role of ocean in the response of tropical climatology to global warming: The west-east SST contrast, *J. Clim.*, *11*, 864–875, doi:10.1175/1520-0442(1998)011<0864:TROOIT>2.0.CO;2.

Liu, Z. (2002), A simple model study of the forced response of ENSO to an external periodic forcing, *J. Clim.*, *15*, 1088–1098, doi:10.1175/1520-0442(2002)015<1088:ASMSOE>2.0.CO;2.

Liu, Z., J. Kutzbach, and L. Wu (2000), Modeling climate shift of El Niño variability in the Holocene, *Geophys. Res. Lett.*, *27*(15), 2265–2268, doi:10.1029/2000GL011452.

Liu, Z., E. Brady, and J. Lynch-Stieglitz (2003), Global ocean response to orbital forcing in the Holocene, *Paleoceanography*, *18*(2), 1041, doi:10.1029/2002PA000819.

Lorenz, S. J., and G. Lohmann (2004), Acceleration technique for Milankovitch type forcing in a coupled atmosphere-ocean circulation model: Method and application for the Holocene, *Clim. Dyn.*, *23*, 727–743, doi:10.1007/s00382-004-0469-y.

Lorenz, S. J., J.-H. Kim, N. Rimbu, R. R. Schneider, and G. Lohmann (2006), Orbitally driven insolation forcing on Holocene climate trends: Evidence from alkenone data and climate modeling, *Paleoceanography*, *21*, PA1002, doi:10.1029/2005PA001152.

Madec, G. (2008), NEMO ocean engine, *Notes Pole Modél. 27*, Inst. Pierre Simon Laplace, Paris.

McPhaden, M. J., et al. (1998), The Tropical Ocean-Global Atmosphere observing system: A decade of progress, *J. Geophys. Res.*, *103*, 14,169–14,240, doi:10.1029/97JC02906.

McPhaden, M. J., S. E. Zebiak, and M. H. Glantz (2006), ENSO as an integrating concept in Earth science, *Science*, *314*, 1740–1745, doi:10.1126/science.1132588.

McWilliams, J., and P. Gent (1978), A coupled air-sea model for the tropical Pacific, *J. Atmos. Sci.*, *35*, 962–989, doi:10.1175/1520-0469(1978)035<0962:ACAASM>2.0.CO;2.

Meehl, G. A., P. R. Gent, J. M. Arblaster, B. L. Otto-Bliesner, E. C. Brady, and A. Graig (2001), Factors that affect the amplitude of El Niño in global climate couple model, *Clim. Dyn.*, *17*, 515–526, doi:10.1007/PL00007929.

Montoya, M., H. von Storch, and T. J. Crowley (2000), Climate simulation for 125 kyr BP with a coupled ocean-atmosphere general circulation model, *J. Clim.*, *13*(6), 1057–1072, doi:10.1175/1520-0442(2000)013<1057:CSFKBW>2.0.CO;2.

Moore, A. M., and R. Kleeman (1999), Stochastic forcing of ENSO by intraseasonal oscillations, *J. Clim.*, *12*, 1199–1220, doi:10.1175/1520-0442(1999)012<1199:SFOEBT>2.0.CO;2.

Moy, C. M., G. O. Seltzer, D. T. Rodbell, and D. M. Anderson (2002), Variability of El Niño–Southern Oscillation activity at millennial timescales during the Holocene epoch, *Nature*, *420*, 162–165, doi:10.1038/nature01194.

Neelin, J. D., M. Latif, and F. F. Jin (1994), Dynamics of coupled ocean-atmosphere models: The tropical problem, *Annu. Rev. Fluid Mech.*, *26*, 617–659, doi:10.1146/annurev.fl.26.010194.003153.

Neelin, J. D., D. S. Battisti, A. C. Hirst, F.-F. Jin, Y. Wakata, T. Yamagata, and S. E. Zebiak (1998), ENSO theory, *J. Geophys. Res.*, *103*(C7), 14,261–14,290, doi:10.1029/97JC03424.

Otto-Bliesner, B., E. Brady, S. Shin, Z. Liu, and C. Shield (2003), Modeling El Niño and its tropical teleconnections during the last glacial-interglacial cycle, *Geophys. Res. Lett.*, *30*(23), 2198, doi:10.1029/2003GL018553.

Otto-Bliesner, B., et al. (2006), Simulating Arctic climate warmth and icefield retreat in the last interglaciation, *Science*, *311*(5768), 1751–1753, doi:10.1126/science.1120808.

Park, W., and M. Latif (2008), Multidecadal and multicentennial variability of the meridional overturning circulation, *Geophys. Res. Lett.*, *35*, L22703, doi:10.1029/2008GL035779.

Park, W., and M. Latif (2010), Pacific and Atlantic multidecadal variability in the Kiel Climate Model, *Geophys. Res. Lett.*, *37*, L24702, doi:10.1029/2010GL045560.

Park, W., and M. Latif (2012), Atlantic Meridional Overturning Circulation response to idealized external forcing, *Clim. Dyn.*, doi:10.1007/s00382-011-1212-0, in press.

Park, W., N. Keenlyside, M. Latif, A. Stroeh, R. Redler, E. Roeckner, and G. Madec (2009), Tropical Pacific climate and its response to global warming in the Kiel Climate Model, *J. Clim.*, *22*, 71–92, doi:10.1175/2008JCLI2261.1.

Penland, C., and P. D. Sardeshmukh (1995), The optimal growth of tropical sea surface temperature anomalies, *J. Clim.*, *8*, 1999–2024, doi:10.1175/1520-0442(1995)008<1999:TOGOTS>2.0.CO;2.

Petit, J. R., et al. (1999), Climate and atmospheric history of the past 420,000 years from the Vostok ice core, Antarctica, *Nature*, *399*, 429–436, doi:10.1038/20859.

Philander, S. G. (1990), *El Niño, La Niña, and the Southern Oscillation*, Academic, London.

Philander, S. G. (1999), A review of tropical ocean-atmosphere interactions, *Tellus B*, *51*, 71–90.

Philip, S. Y., and G. J. van Oldenborgh (2006), Shifts in ENSO coupling processes under global warming, *Geophys. Res. Lett.*, *33*, L11704, doi:10.1029/2006GL026196.

Rayner, N. A., D. E. Parker, E. B. Horton, C. K. Folland, L. V. Alexander, D. P. Rowell, E. C. Kent, and A. Kaplan (2003), Global analyses of sea surface temperature, sea ice, and night marine air temperature since the late nineteenth century, *J. Geophys. Res.*, *108*(D14), 4407, doi:10.1029/2002JD002670.

Rodbell, D. T., G. O. Seltzer, D. M. Anderson, M. B. Abbott, D. B. Enfield, and J. H. Newman (1999), An ~15,000-year record of El Niño-driven alluviation in southwestern Ecuador, *Science*, *283*, 516–520, doi:10.1126/science.283.5401.516.

Roeckner, E., R. Brokopf, M. Esch, M. Giorgetta, S. Hagemann, L. Kornblueh, E. Manzini, U. Schlese, and U. Schulzweida (2003), The atmospheric general circulation model ECHAM5. Part I: Model description, *Tech Rep. 349*, Max Planck Inst. für Meteorol., Hamburg, Germany.

Ropelewski, C. F., and M. S. Halpert (1996), Quantifying Southern Oscillation-precipitation relationships, *J. Clim.*, *9*, 1043–1059, doi:10.1175/1520-0442(1996)009<1043:QSOPR>2.0.CO;2.

Schneider, B., G. Leduc, and W. Park (2010), Disentangling seasonal signals in Holocene climate trends by satellite-model-proxy integration, *Paleoceanography*, *25*, PA4217, doi:10.1029/2009PA001893.

Shulmeister, J., and B. G. Lees (1995), Pollen evidence from tropical Australia for the onset of an ENSO-dominated climate at c. 4000 BP, *Holocene*, *5*, 10–18, doi:10.1177/095968369500500102.

Stenseth, N. C., A. Mysterud, G. Ottersen, J. W. Hurrell, K.-S. Chan, and M. Lima (2002), Ecological effects of climate fluctuations, *Science*, *297*, 1292–1296, doi:10.1126/science.1071281.

Stirling, C. H., T. M. Esat, K. Lambeck, and M. T. McCulloch (1998), Timing and duration of the last interglacial: Evidence for a restricted interval of widespread coral reef growth, *Earth Planet. Sci. Lett.*, *160*, 745–762, doi:10.1016/S0012-821X(98)00125-3.

Thompson, C. J., and D. S. Battisti (2001), A linear stochastic dynamical model of ENSO. Part II: Analysis, *J. Clim.*, *14*, 445–466, doi:10.1175/1520-0442(2001)014<0445:ALSDMO>2.0.CO;2.

Timmermann, A., S. Lorenz, S. I. An, A. Clement, and S.-P. Xie (2007), The effect of orbital forcing on the mean climate and variability of the tropical Pacific, *J. Clim.*, *20*, 4147–4159, doi:10.1175/JCLI4240.1.

Tudhope, A. W., C. P. Chilcott, M. T. McCulloch, E. R. Cook, J. Chappell, R. M. Ellam, D. W. Lea, J. M. Lough, and G. B. Shimmield (2001), Variability in the El Niño–Southern Oscillation through a glacial-interglacial cycle, *Science*, *291*, 1511–1517, doi:10.1126/science.1057969.

Valcke, S. (2006), OASIS3 user guide, *PRISM Tech. Rep. 3*, 78 pp., Program for Integr. Earth Syst. Model., Hamburg, Germany. [Available at http://www.prism.enes.org/Publications/Reports/all_editions/oasis3_UserGuide_No2_3.pdf.]

Voss, R., and U. Mikolajewicz (2001), The climate of 6000 years BP in near-equilibrium simulations with a coupled AOGCM, *Geophys. Res. Lett.*, *28*(11), 2213–2216, doi:10.1029/2000GL012498.

Wang, C., and J. Picaut (2004), Understanding ENSO physics—A review, in *Earth's Climate: The Ocean-Atmosphere Interaction*, *Geophys. Monogr. Ser.*, vol. 147, edited by C. Wang, S.-P. Xie, and J. A. Carton, pp. 21–48, AGU, Washington, D. C., doi:10.1029/147GM02.

Zavala-Garay, J., A. M. Moore, C. L. Perez, and R. Kleeman (2003), The response of a coupled mode of ENSO to observed estimates of stochastic forcing, *J. Clim.*, *16*, 2827–2842, doi:10.1175/1520-0442(2003)016<2827:TROACM>2.0.CO;2.

Zebiak, S., and M. Cane (1987), A model El Niño–Southern Oscillation, *Mon. Weather Rev.*, *115*(10), 2262–2278, doi:10.1175/1520-0493(1987)115<2262:AMENO>2.0.CO;2.

Zeng, N., and J. D. Neelin (2000), The role of vegetation-climate interaction and interannual variability in shaping the African Savanna, *J. Clim.*, *13*, 2665–2670, doi:10.1175/1520-0442(2000)013<2665:TROVCI>2.0.CO;2.

Zheng, W., P. Braconnot, E. Guilyardi, U. Merkel, and Y. Yu (2008), ENSO at 6 ka and 21 ka from ocean–atmosphere coupled model simulations, *Clim. Dyn.*, *30*, 745–762, doi:10.1007/s00382-007-0320-3.